

Chapter 3

Aluminum Foam-Filled Circular-Triangular Nested Tubes Under Impact



3.1 Introduction

Thin-walled empty or foam-filled metallic tubes were widely employed as energy absorbers to dissipate impact energy owing to their easy fabrication and desirable energy absorption performance. The axial crushing performances of empty or foam-filled metallic tubes generally outperformed the laterally loaded counterparts in terms of enhanced energy absorption capacity (Baroutaji et al. 2017). However, fewer fluctuation of crushing force and more stable deformation mode were observed for the “tube-type” energy absorbers under lateral loading (Tran 2017) or with windowed shaped cuttings (Tran et al. 2021). The laterally loaded empty or foam-filled metallic tubes could be the desirable energy absorbers if their energy absorptions could be enhanced. Hence, the nested tubes and the tubes with constraints or functionally graded thickness were generally proposed for improving energy absorption capacity (Nikkhah et al. 2020; Baroutaji et al. 2021). Recently, a new circular-triangular nested tube (CTNT) energy absorber was proposed by the authors (Wang et al. 2020a), and the constraints between circular and triangular tubes were found to evidently enhance its energy absorption capacity. In this study, the CTNT energy absorber was filled with aluminum foam to further improve its energy absorption performance, as shown in Fig. 3.1. With the aim of using the proposed aluminum foam-filled circular-triangular nested tube (AFCTNT) energy absorber to further improve the energy absorption performance of the CTNT energy absorber, this work is of significance for revealing the energy absorption behavior of the AFCTNT energy absorber under impact loading and facilitating its application in impact energy dissipation.

The responses of circular tubes under lateral crushing have been extensively studied as they generally exhibited stable energy dissipation (Gupta et al. 2005). The formulae for calculating the force–displacement responses of the laterally loaded circular tubes were also developed (Wang 1987; McDevitt and Simmonds 2003), which could be used to assess their energy absorption performances. The dynamic lateral crushing behavior of circular tubes was also studied by Fan et al. (2013) as the energy absorbers were generally employed for dissipating impact or blast energy.

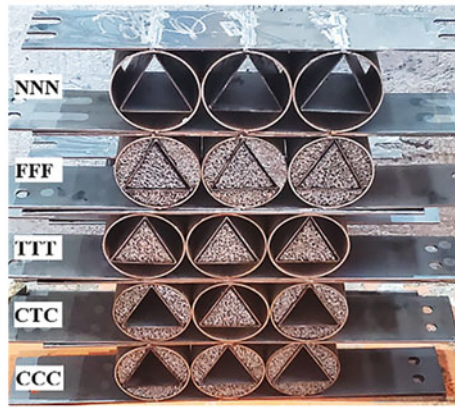
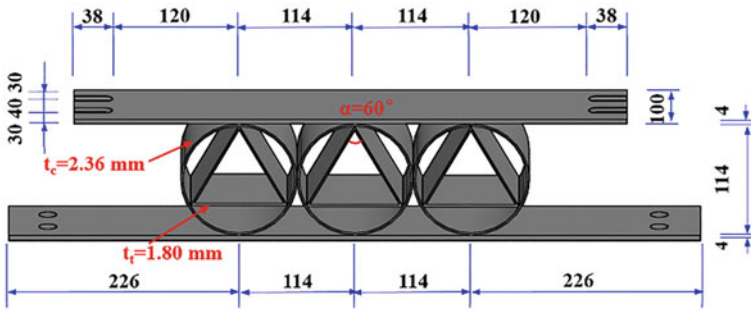


Fig. 3.1 Geometry of the AFCTNT energy absorbers (mm), reprinted from Wang et al. (2021), copyright 2022, with permission from Elsevier

It was found that the inertial effect induced by dynamic loading could result in the change of deformation modes of the circular tubes, which together with strain rate effect could enhance their energy absorption capacities (Su et al. 1995a, b). In addition, rectangular, triangular and elliptical tubes could also be employed for dissipating impact or blast energy and its response under lateral crushing was also extensively studied (Gupta et al. 2001; Wu and Carney 1997; Tran and Ton 2016; Fan et al. 2015). The laterally loaded triangular tubes generally exhibited improved energy absorption capacity comparing with circular tubes, and three deformation modes and a unified energy dissipation mechanism were observed by Wang et al. (2015). However, larger initial peak force was observed for the triangular tube, which could reduce its energy absorption efficiency. External constraints or nested tubes were widely adopted to enhance the energy absorption performance of the single tube. It was found that the energy absorption of a circular tube subjected to lateral loading was improved with the presence of external constraints owing to more severe plastic deformation as compared to the counterparts without external constraints (Reid et al. 1983; Reddy and Reid 1979). With regard to the nested tubes which consist of at least two tubes, significant improvement in energy absorption performance could also be observed

(Morris et al. 2006). The behavior of nested tubes under lateral dynamic loading was studied (Baroutaji et al. 2016; Olabi et al. 2008), and the improved energy absorption performance of the nested tubes could be observed through optimized design.

Recently, aluminum foam was increasingly employed as the filler of a metallic tube to enhance its energy absorption performance owing to the light weight, high specific energy absorption and stable energy dissipation of aluminum foam. Till date, a considerable amount of studies have been conducted to reveal the behavior of aluminum foam-filled energy absorbers under axial (Duarte et al. 2015; Shahbeyk et al. 2007) or oblique (Reyes et al. 2004) crushing. It was found that the energy absorption performance could be evidently improved by filling tubes with aluminum foam (Santosa et al. 2000). In addition, the foam filler was found to stabilize the deformation mode and enhance the energy absorption capacity through investigating the axially loaded foam-filled conical tubes (Ahmad and Thambiratnam 2009). To smooth the crushing force–displacement curve and reduce the initial peak force, the aluminum foam-filled corrugated tubes were proposed, and its behavior under dynamic crushing was also studied (Kilicaslan 2015). The results indicated that aluminum foam-filled corrugated tubes experienced progressive and concertina type of deformation mode. A new dual functionally graded structure with variation of both foam density and tube wall thickness was proposed by Fang et al. (2016), and the improved energy absorption performance was demonstrated by comparing with the uniform counterparts. The multi-objective optimisation design (MOD) of foam-filled tubes under oblique impact loading was conducted to enhance their crashworthiness (Yang and Qi 2013; Qi and Yang 2014). It was found that more robust designs could be achieved by incorporating multiple load angles into the MOD process (Yang and Qi 2013). With regard to the lateral crushing behavior of foam-filled tubes, smoother crushing force–displacement responses could be observed as compared to the axially loaded counterparts (Shen et al. 2015). The energy absorption performances of sandwich tubes under dynamic lateral crushing were studied by Fan et al. (2013), and different deformation modes of the sandwich tubes between the dynamic and quasi-static loading cases could be observed owing to the inertial effect. Further, MOD was employed for finding the optimal configuration of laterally loaded sandwich tubes, and the tube with a minimum diameter of inner layer and a maximum foam thickness was found to be more desirable (Baroutaji et al. 2015). Up to date, no study has been performed on the new aluminum foam-filled nested system presented in this chapter, which is composed of circular tubes, triangular tubes, and aluminum foam.

A new AFCTNT energy absorber was proposed for improving the energy absorption performance of the recently developed CTNT energy absorber. Drop-weight impact tests on the AFCTNT energy absorbers with different volumes of aluminum foam filler were first conducted to reveal their energy absorption performances. In addition, numerical simulations on the AFCTNT energy absorbers under impact loading were also carried out by employing the explicit code in LS-DYNA, and more in-depth discussions on the impact behavior of the AFCTNT energy absorbers were presented based on the numerical results.

3.2 Methodologies

3.2.1 Experimental Methodology

3.2.1.1 Specimens

The AFCTNT energy absorber specimens prepared for the drop-weight impact tests are presented in Fig. 3.1. Five types of AFCTNT energy absorbers are designed with the variation of aluminum foam volume, and the notations of the specimens are illustrated in Fig. 3.1. Two identical energy absorbers of each type of specimens were fabricated for validating the repeatability of the experimental results. The CTNT energy absorber includes two flat plates, three circular tubes, and three triangular tubes, as shown in Fig. 3.1. The fabrication process of the CTNT energy absorber includes: (a) welding three steel plates with equal lengths together to form the inner triangular tube with cross-section to be an equilateral triangle, (2) filling three triangular tubes into three circular tubes, and (3) fixing the circular tubes to the top and bottom flat plates through welding. Finally, the CTNT energy absorbers were filled with aluminum foam, and different volumes of aluminum foam filler were chosen for revealing its influence on the behavior of the AFCTNT energy absorber. The geometries of the specimens are presented in Fig. 3.1. All the specimens share the same geometries of the CTNT energy absorber with width and outer diameter of circular tubes to be 100 and 114 mm, respectively. The measured thicknesses of circular and triangular tubes are 2.36 and 1.80 mm, respectively. The material properties of mild steel and aluminum foam employed for the specimens are given in Table 3.1.

3.2.1.2 Experimental Setup and Instrumentation

The impact tests on the AFCTNT energy absorbers were carried out via employing a drop-weight impact test system, and Fig. 3.2 presents the test setup and instrumentation. The drop-weight impact test system mainly includes a hammer with adjustable weight from 400 to 1000 kg, a hydraulic-controlled mechanical hosting system, two guide rails, a dynamic load cell, a high-speed camera, and two lights. The hammer

Table 3.1 Material parameters of mild steel and aluminum foam

Mild steel	E_y (GPa)	σ_y (MPa)	σ_u (MPa)
$t_p = 1.80$ mm	200	292	433
$t_p = 2.36$ mm	200	294	393
Aluminum foam	ρ_f (g/cm ³)	σ_p (MPa)	E_f (MPa)
–	0.28	2.87	207.8

Note E_y , E_f –Young’s modulus of steel and aluminum foam; σ_y , σ_u –Yield and ultimate stress of steel; ρ_f , σ_p –Density and plateau stress of aluminum foam

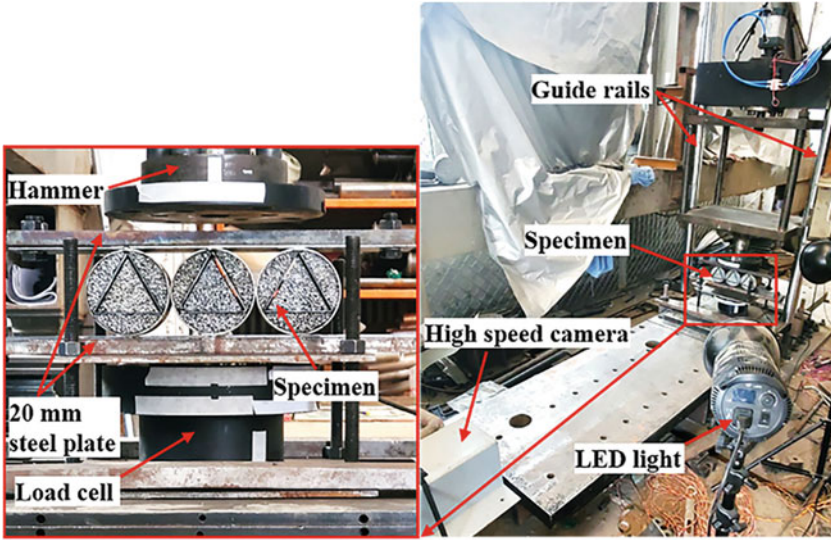


Fig. 3.2 Test setup of AFCTNT energy absorber, reprinted from Wang et al. (2021), copyright 2022, with permission from Elsevier

can be lift up to 20 m using the hosting system. It drops freely along the guide rails and strikes the specimens once the electromagnet release mechanism is triggered. The dynamic load cell is installed below the specimen to measure the pure impact force and remove the inertial force from the measurement. The top and bottom plates of the AFCTNT energy absorbers are enhanced with two steel plates with thickness of 20 mm through bolting connection for preventing plastic deformation of these two plates and assuring the impact energy only dissipated through circular tubes, triangular tubes, and aluminum foam. The total drop weight was 400 kg, and the drop heights of the specimens presented in Table 3.2 were determined based on trial numerical simulations, assuring the specimens reaching densification and maximum impact force being smaller than 2000 kN (the maximum measurement range of the dynamic load cell). The high-speed camera was employed to capture the crushing process of the specimen and movement of the hammer at a speed of 3000 frames per second.

3.2.2 Numerical Methodology

The numerical simulations on the AFCTNT energy absorbers under impact loading were performed by employing the explicit code in LS-DYNA (Hallquist 2006). Figure 3.3 presents the FE model of the specimen FFF with fully-filled aluminum foam under impact loading. The aluminum foam and hammer were meshed with

Table 3.2 Energy absorption parameters of the energy absorbers ($\delta = 63$ mm)

Specimen	H_d (m)	EA (kJ)	SEA (kJ/kg)	MCF (kN)	CFE
NNN-1	3	5.87	1.90	93.17	0.46
NNN-2	3	6.49	2.09	102.92	0.42
NNN-mean	–	6.18	2.00	98.04	0.44
TTT-1	4	9.18	2.74	145.63	0.58
TTT-2	4	9.90	2.96	157.11	0.49
TTT-mean	–	9.54	2.85	151.37	0.53
CCC-1	4	10.40	2.94	165.01	0.67
CCC-2	4	10.12	2.86	160.52	0.60
CCC-mean	–	10.26	2.90	162.76	0.64
CTC-1	4	8.74	2.52	138.74	0.66
CTC-2	4	8.88	2.56	140.78	0.61
CTC-mean	–	8.81	2.54	139.76	0.63
FFF-1	4.3	15.04	3.97	238.69	0.56
FFF-2	5	14.76	3.90	233.96	0.67
FFF-mean	–	14.90	3.93	236.32	0.62

Note H_d —Drop height; EA —Energy absorption; SEA —Specific energy absorption; MCF —Mean crushing force; CFE —Crushing force efficiency

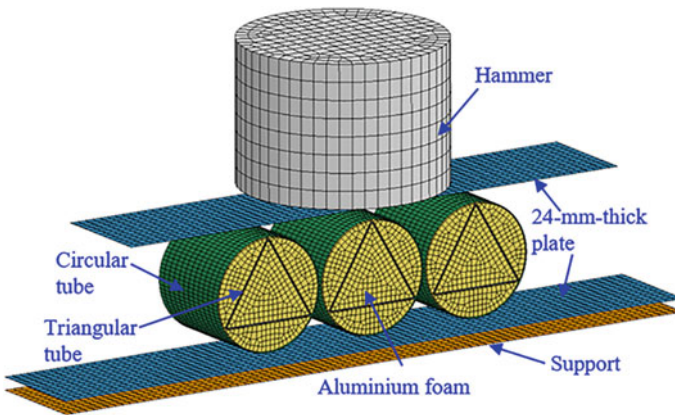
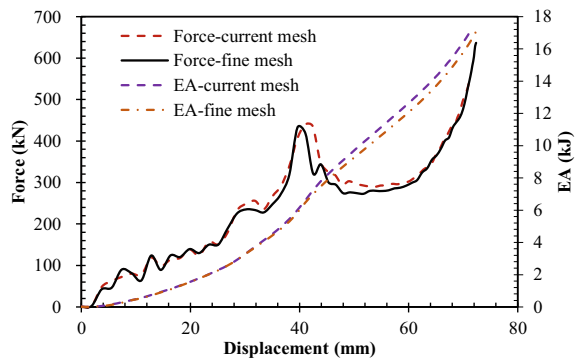


Fig. 3.3 FE model of the specimen FFF under impact loading, reprinted from Wang et al. (2021), copyright 2022, with permission from Elsevier

8-node solid elements, and reduced integration of the solid element was employed to reduce computation time. The Belytschko-Tsay shell element was employed for meshing circular and triangular tubes, flat plates and support, and five integration points were specified along thickness of the shell element. The stiffness-based hourglass control was employed for prohibiting the zero-energy deformation modes of

the elements with reduced integration. The mesh size of 4 mm was chosen for the circular tubes, triangular tubes and aluminum foam which experienced severe plastic deformation during impact, and 8 mm mesh size was adopted for the support and flat plates. The current mesh sizes in the FE modeling were chosen based on the mesh sensitivity analysis. The FE model of the specimen FFF with fine mesh sizes (by halving the current mesh sizes) was also established, and the FE-predicted energy absorption and force versus displacement curves were found to be close on employing the two mesh sizes, as presented in Fig. 3.4. Therefore, the current mesh sizes were adopted for the following numerical simulations in this study, which could assure both the accuracies of the FE results and reasonable computation time. The contacts between two parts of the FE model were simulated utilizing the “automatic surface to surface” option in LS-DYNA. The penalty-based contact approach was employed for the contact pairs with steel material (i.e., hammer, flat plate, circular tube, triangular tube and support), since its contact stiffness is determined by an algorithm based on the sizes and material properties of contact segments and it works more effectively when the material stiffness parameters between the contacting surfaces are of the same order-of-magnitude. The contact between aluminum foam and metallic tubes was modeled through the soft constraint-based contact approach, whose contact stiffness is independent of material parameters and suited for treating the contact between materials of different stiffness parameters (i.e., aluminum foam and steel plate). The fixed boundary condition was applied to the support, and all the degrees of freedom of the nodes on the hammer were constrained except for the vertical direction. The initial impact velocity of the hammer was specified via the keyword “*Initial_Velocity_Generation”. The welding connections between the circular tubes and flat plates were modeled through tying the nodes on the welding zone of circular tubes to flat plates, since welding connection failure was not observed from the drop-weight impact tests. The 4-mm-thick top and bottom steel plates were bolted to the two 20-mm-thick steel plates in the test setup, and no bolting connection failure was observed from the tests. Hence, the 24-mm-thick steel plates were adopted in the FE model to replace the two flat plates (with thickness of 4 and 20 mm, respectively) connected by bolts (Fig. 3.3).

Fig. 3.4 Mesh sensitivity analysis of AFCTNT energy absorber, reprinted from Wang et al. (2021), copyright 2022, with permission from Elsevier



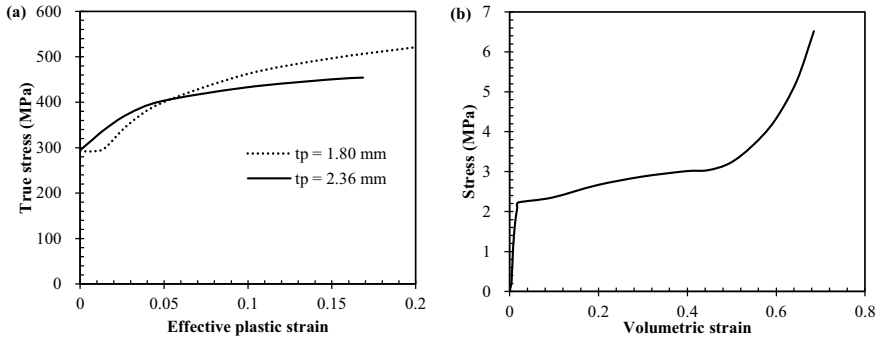


Fig. 3.5 Stress–strain curves defined in the FE model: **a** mild steels and **b** aluminum foam, reprinted from Wang et al. (2021), copyright 2022, with permission from Elsevier

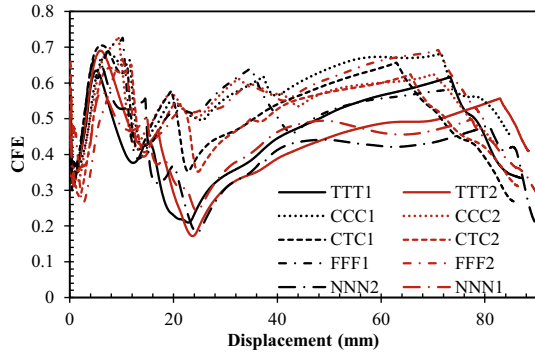
The Piecewise Linear Plasticity model (MAT_24 in LS-DYNA) was employed in the FE model to simulate steel materials of the AFCTNT energy absorber. The strain rate effect was considered in this model via employing the Cowper-Symonds model, and the strain rate parameters C and P are defined as 40.4 s^{-1} and 5 for mild steel (Jones 1988). The material properties of circular and triangular tubes defined in the FE model were obtained from tensile coupon tests and presented in Table 3.1, and the true stress–effective plastic strain curves are presented in Fig. 3.5a. The Crushable Foam material model (MAT_63), which showed desirable performance and high computational efficiency (Hanssen et al. 2002), was adopted for simulating aluminum foam. The input stress–volumetric strain curve for aluminum foam was obtained from the uniaxial compressive loading tests and given in Fig. 3.5b. The plastic Poisson’s ratio of aluminum foam was defined to be 0.01 (Qi et al. 2018; Yang and Qi 2013) as the lateral expansion of aluminum foam under uniaxial compressive loading was found to be minimal (Song et al. 2005).

3.3 Results and Discussions

3.3.1 Energy Absorption Parameters

The energy absorption parameters, e.g., energy absorption (EA), specific energy absorption (SEA), mean crushing force (MCF), and crushing force efficiency (CFE), were generally employed for quantitatively assessing the energy absorption performances of energy absorbers. All the aforementioned energy absorption parameters can be calculated based on crushing force–displacement curve of the energy absorber and are given in Eqs. (1.1)–(1.4). The CFE –displacement curve is employed herein to determine the densification displacement of the AFCTNT energy absorber, and

Fig. 3.6 *CFE*–displacement curves of all the specimens, reprinted from Wang et al. (2021), copyright 2022, with permission from Elsevier



its densification is reached when *CFE* exhibits continuous and sudden drop (Wang et al. 2019). In addition, an identical densification displacement should be chosen for all the specimens to assure a faire comparison of their energy absorption performances. As illustrated in Fig. 3.6, the minimum densification displacement of all the ten specimens (63 mm) was chosen to assure all the specimens reaching densification after this value. Table 3.2 presents the energy absorption parameters of all the tested energy absorbers corresponding to crushing displacement of 63 mm.

3.3.2 FE Model Validation

Figure 3.7 provides a comparison of deformation modes of the AFCTNT energy absorbers obtained from FE simulations and drop-weight impact tests, and the FE-predicted deformation modes are found to be consistent with those from the tests. Plastic deformations of the circular and triangular tubes as well as crushing of the aluminum foam can be reasonably captured by the established FE models, including plastic hinge lines and curvature change of nested tubes, buckling modes of triangular tubes, inner surface contacts of nested tubes, and aluminum foam densification. However, There are slightly different deformation modes of the specimen NNN between the test and FE prediction being observed, i.e., the buckling direction of the triangular tube from the FE simulation is not consistent with that from the test. This may be caused by the geometrical imperfection of the fabricated specimen (Wang et al. 2020a), and the buckling direction of the triangular tube is random. The buckling direction of triangular tube has little effect on the energy absorption as the unsymmetrical deformation mode of the triangular tube is observed from both the test and FE prediction. The detailed discussions on the crushing processes of the energy absorbers are given in Sect. 3.3.3.

Figure 3.8 presents a comparison of *EA*–displacement curves obtained from the tests and FE analyses, and good agreement between them can be observed. Generally, the FE-predicted *EA* is found to be slightly smaller than that from tests. In addition, a comparison of force–displacement curves obtained from the tests and FE analyses

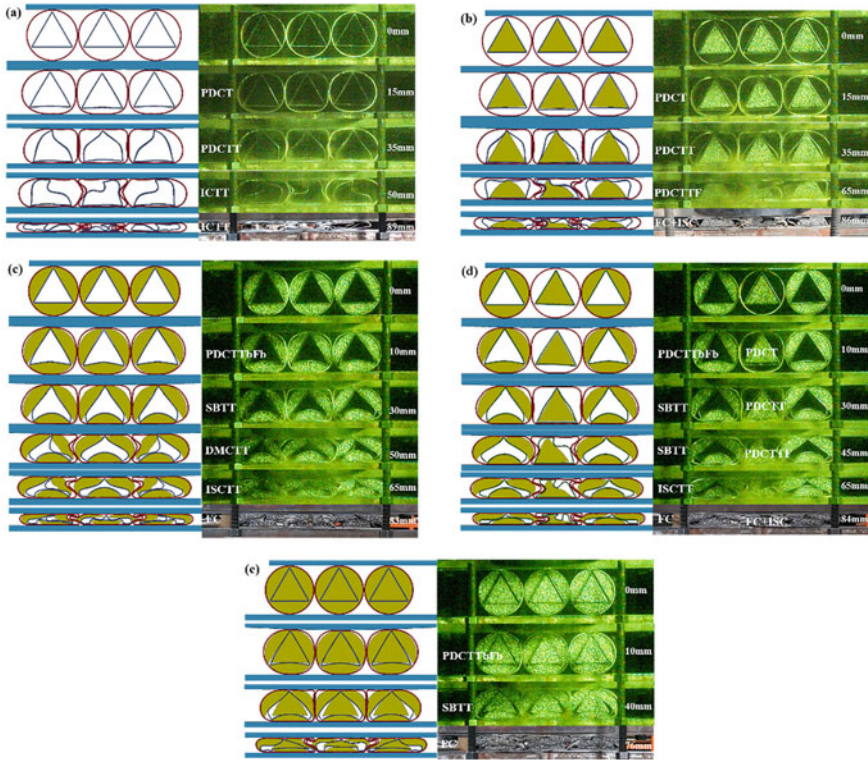
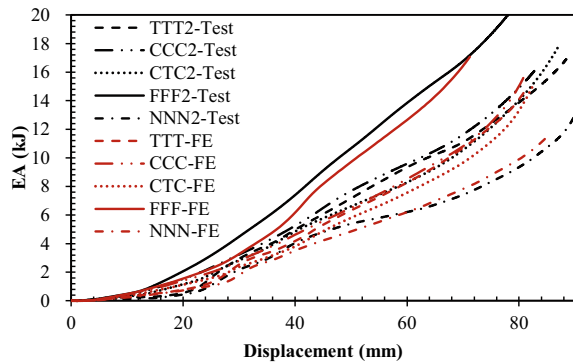


Fig. 3.7 Crushing processes of AFCTNT energy absorbers under impact load: **a** NNN, **b** TTT, **c** CCC, **d** CTC and **e** FFF (PDCT—plastic deformation of only circular tubes; PDCTT—plastic deformation of both circular and triangular tubes; ICTT—interaction between circular and triangular tubes; ISC—inner surface contact; PDCTTF—plastic deformation of circular and triangular tubes and aluminum foam; FC + ISC—aluminum foam compaction and inner surface contact; PDCT-TbFb—plastic deformation of circular tubes, bottom sides of triangular tubes and aluminum foam at bottom; SBTT—symmetrical buckling of triangular tubes; DMCTT—deformation mode change of outer triangular tubes; ISCTT—inner surface contacts of triangular tubes; FC—aluminum foam compaction), reprinted from Wang et al. (2021), copyright 2022, with permission from Elsevier

Fig. 3.8 Comparison of EA—displacement curves obtained from tests and FE simulations, reprinted from Wang et al. (2021), copyright 2022, with permission from Elsevier



is also presented in Fig. 3.9, which further confirms the reasonable predictions from FE models. The slight differences of force–displacement curves between the tests and FE predictions may be caused by geometric imperfections of the fabricated specimens. The aforementioned comparisons of deformation modes as well as force and energy absorption versus displacement curves between the tests and FE simulations demonstrate that the FE modeling of the AFCTNT energy absorber under impact loading is acceptable and can be employed for further analysis.

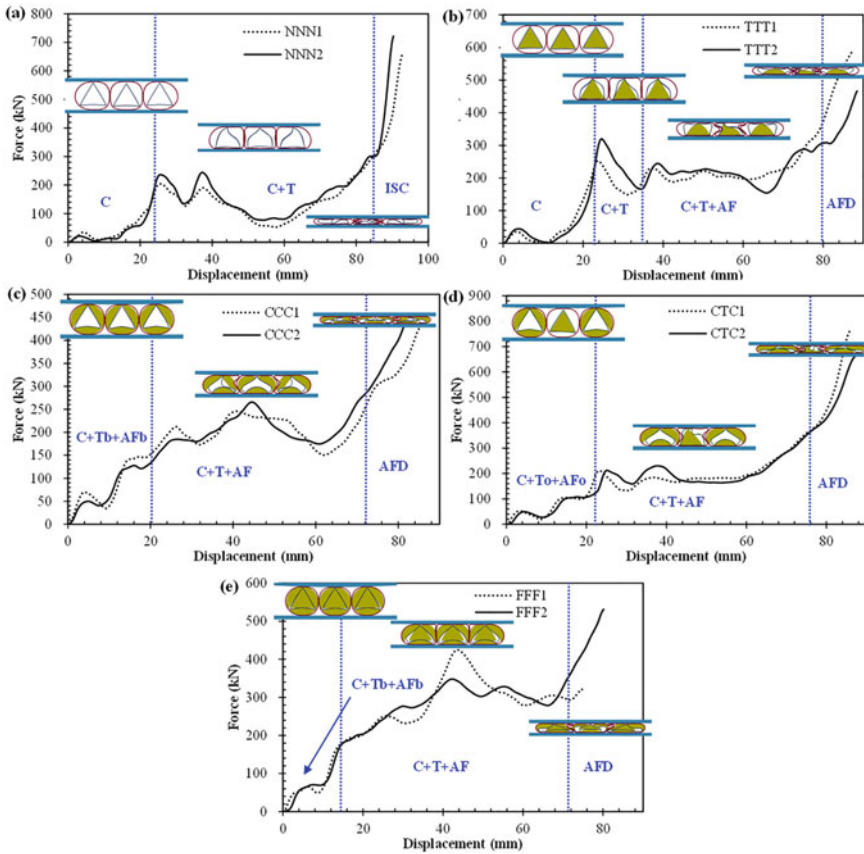


Fig. 3.9 Force–displacement curves of the AFCTNT energy absorbers: **a** NNN, **b** TTT, **c** CCC, **d** CTC and **e** FFF. (C—Energy dissipation by circular tubes; C + T—Energy dissipation by circular and triangular tubes; C + T + AF—Energy dissipation by circular and triangular tubes as well as aluminum foam; AFD—Aluminum foam densification; C + To + AFo—Energy dissipation by circular tubes as well as triangular tubes and AF of two outer units; C + Tb + AFb—Energy dissipation by circular tubes as well as bottom side of triangular tubes and AF at the bottom; ISC—Inner surface contact), reprinted from Wang et al. (2021), copyright 2022, with permission from Elsevier

3.3.3 Deformation Mode

Figure 3.7 presents the crushing processes of the tested AFCTNT energy absorbers subjected to impact loading. For the specimen NNN without aluminum foam, the impact energy is dissipated through plastic deformation of circular and triangular tubes, and four crushing stages are identified (Wang et al. 2020a). Only circular tubes exhibit plastic deformation at initial crushing stage ($\delta = 15$ mm in Fig. 3.7a), and the interaction between adjacent circular tubes is achieved via assembling the circular tubes to be contacted with each other, and meanwhile welding the circular tubes to the top and bottom flat plates. This results in higher energy absorption than that of circular tubes without constraints. The inclined sides of triangular tubes start to buckle and absorb impact energy via plastic deformation with further crushing, and both symmetrical and asymmetrical deformation modes of the three triangular tubes are observed after buckling ($\delta = 35$ mm in Fig. 3.7a). When $\delta = 50$ mm, the triangular tubes contact with circular tubes, and the interaction between triangular and circular tubes can be observed, which leads to the deformation mode change of the middle triangular tube (from a symmetrical mode to an asymmetrical one). Finally, the inner surface contacts of triangular tubes occurs, which leads to densification of the specimen ($\delta = 89$ mm in Fig. 3.7a).

As for the specimen TTT with aluminum foam only being filled in three triangular tubes, four different crushing stages can also be found. The deformation modes of the specimen TTT at the first and second crushing stages are similar to those of specimen NNN without aluminum foam filler, i.e., plastic deformation of only circular tubes and plastic deformation of both circular and triangular tubes for the first and second crushing stage, respectively ($\delta = 15$ and 35 mm, respectively, in Fig. 3.7b). Herein, all the triangular tubes exhibit asymmetrical deformation mode after buckling. With further crushing of the specimen TTT, aluminum foam starts to experience evident compaction and dissipate impact energy ($\delta = 65$ mm in Fig. 3.7b). Moreover, the interactions between the triangular tubes and aluminum foam as well as between the triangular and circular tubes are also observed, which can improve the energy absorption capacity of the specimen. The densification of specimen TTT is reached after complete compaction of aluminum foam and inner surface contacts of nested tubes ($\delta = 86$ mm in Fig. 3.7b).

Figure 3.7c presents the crushing processes of the specimen CCC with aluminum foam only being filled in the gaps between the circular and triangular tubes, and five crushing stages can be observed. At initial crushing stage ($\delta = 10$ mm in Fig. 3.7c), plastic deformation of the circular tubes and bottom sides of the triangular tubes can be observed, and meanwhile aluminum foam below the bottom sides of triangular tubes also exhibits evident compaction. All the triangular tubes then experience symmetrical deformation mode after buckling, and the plastic deformation occurs at the inclined sides of triangular tubes with further crushing of the specimen ($\delta = 30$ mm in Fig. 3.7c). The determined symmetrical deformation mode of triangular tubes at this crushing stage is believed to be triggered by upward bending of the bottom sides of triangular tubes. When crushing displacement is 50 mm, concavity

of the two outer circular tubes at the contacted surfaces is developed, which results in the change of deformation mode of the two outer triangular tubes, i.e., from a symmetrical mode to an asymmetrical one. With continuous crushing, inner surface contacts of triangular tubes occur when crushing displacement is 65 mm. After that, aluminum foam exhibits more rapid crushing, and densification of the specimen is reached with complete compaction of aluminum foam ($\delta = 83$ mm in Fig. 3.7c).

The crushing processes of the specimen CTC under impact loading is presented in Fig. 3.7d. Aluminum foam is filled in the middle triangular tube as well as in the gaps between the circular and triangular tubes of the two outer nested tubes. With regard to the deformation modes of the specimen CTC, the two outer nested tubes with aluminum foam filled in the gaps between the circular and triangular tubes exhibit similar deformation modes to those of specimen CCC, while the deformation modes of the middle nested tubes with aluminum foam filled in the triangular tube is consistent with those of specimen TTT. Figure 3.7e presents the crushing processes of the specimen FFF with fully-filled aluminum foam, and three crushing stages can be identified. Similar to the deformation mode of the specimen CCC at initial crushing stage, the specimen FFF also exhibits plastic deformations of circular tubes, bottom sides of triangular tubes, and aluminum foam below the bottom sides of triangular tubes at initial crushing stage ($\delta = 10$ mm in Fig. 3.7e). Subsequently, symmetrical deformation mode of all three triangular tubes after buckling is observed with further crushing, similar to the deformation mode of specimen CCC at the second crushing stage. Meanwhile, all the aluminum foam fillers exhibit evident compaction at $\delta = 40$ mm. Finally, densification of the specimen FFF is reached after complete compaction of aluminum foam.

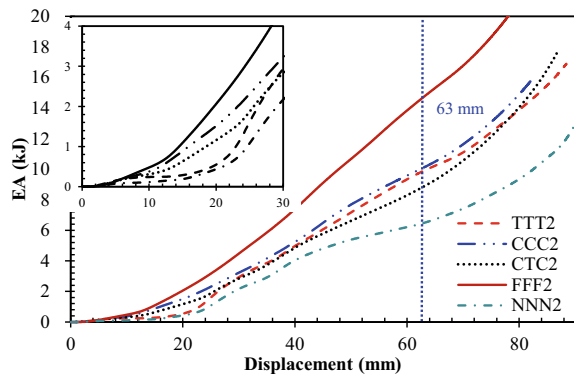
3.3.4 Force and Energy Absorption Responses

The force–displacement responses of the AFCTNT energy absorbers under impact loading are presented in Fig. 3.9, and the repeatability of the experimental data can be confirmed. Figure 3.9a presents the force–displacement curves of the specimen NNN without aluminum foam, and three stages can be identified based on its energy absorption characteristic. The specimen NNN exhibits low crushing force and energy absorption at initial stage, since only plastic deformation of circular tubes contributes to the energy absorption. The crushing force exhibits rapid increase with displacement exceeding 20 mm, which indicates that the inclined sides of the triangular tubes start to resist impact force and buckle after the first peak force. Subsequently, plastic deformation of both circular and triangular tubes contributes to the energy dissipation, which leads to larger crushing force as compared to the initial stage. Finally, rapid and continuous increase of crushing force is observed when inner surface contacts of the tubes occur, and densification of the specimen NNN is reached. With regard to the specimen TTT, the first two stages of the force–displacement response are similar to those of specimen NNN, i.e., only plastic deformation of circular tubes contributing to energy dissipation at the first stage and the following energy

dissipation via plastic deformation of both circular and triangular tubes at the second stage. The aluminum foam starts to undergo evident compaction and dissipate impact energy when displacement exceeds 35 mm. It enters the third stage, and energy dissipation is contributed by circular and triangular tubes as well as aluminum foam. The crushing force also exhibits sudden increase after densification of the specimen when complete compaction of aluminum foam occurs. For the specimens CCC, CTC and FFF which exhibit similar force–displacement response, three stages can be identified from their force–displacement curves. At the initial stage, the force–displacement curves of the specimens CCC and FFF are similar owing to their similar energy dissipation manners, i.e., plastic deformations of circular tubes, bottom sides of triangular tubes, and aluminum foam below the bottom sides of triangular tubes. With regard to the specimen CTC at the initial stage, lower crushing force as compared to specimens CCC and FFF can be observed because the triangular tubes and aluminum foam filled in the middle triangular tube of the specimen CTC have not contributed to energy dissipation at the initial stage. The three specimens (CCC, CTC and FFF) share similar energy dissipation at the second and third stages, i.e., energy dissipation from the circular and triangular tubes, and aluminum foam at the second stage, followed by densification of the specimen induced by aluminum foam compaction at the third stage. It is also noted in Fig. 3.9 that filling aluminum foam in the gaps between the circular and triangular tubes can reduce the peak buckling force, i.e., the specimens CCC, CTC and FFF exhibit smaller peak buckling forces and smoother force–displacement curves as compared to specimens NNN and TTT.

Figure 3.10 presents a comparison of EA –displacement curves of the AFCTNT energy absorbers with variation in aluminum foam volume. All the specimens initially exhibit low energy dissipation rate because the triangular tubes and aluminum foam fillers have not underwent plastic deformation and dissipated impact energy at the initial stage, as discussed in Sect. 3.3.3. Generally, the AFCTNT energy absorber with larger volume of aluminum foam exhibits higher EA , except for specimens CTC and TTT. EA of the specimen TTT with smaller volume of aluminum foam is higher than that of specimen CTC with displacement ranging from 37 to 78 mm. However, the specimen CTC exhibits higher EA than that of specimen TTT at the

Fig. 3.10 Comparison of EA –displacement curves from the five types of energy absorbers, reprinted from Wang et al. (2021), copyright 2022, with permission from Elsevier



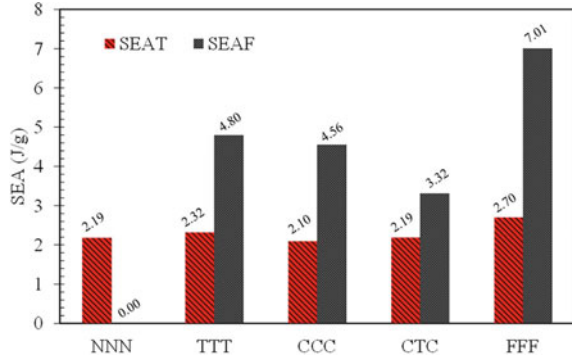
initial and final crushing stages. It can be concluded that filling the energy absorber with aluminum foam is an effectively way to improve its energy absorption performance. The comparison of EA –displacement curves between the specimen NNN and TTT in Fig. 3.10 reveals that energy absorptions of the two specimens are similar at the initial crushing stage and the specimen TTT exhibits higher EA when displacement exceeds 20 mm. This is because the aluminum foam filled in triangular tubes only experiences evident compaction and start to dissipate energy with displacement exceeding 20 mm. This also leads to similar EA of specimen FFF and CCC at the initial crushing stage when displacement is smaller than 15 mm, as can be seen in Fig. 3.10. With further crushing, the specimen FFF with fully-filled aluminum foam exhibits higher EA as compared to the specimen CCC when the aluminum foam filled in triangular tubes initiates energy dissipation. Hence, it can be concluded that the aluminum foam filled in the gaps between circular and triangular tubes experiences earlier compaction as compared to that filled in the triangular tubes. In addition, EA of aluminum foam filled in the gaps between circular and triangular tubes is found to be higher as compared to that filled in triangular tubes owing to its larger volume of aluminum foam.

3.3.5 Energy Absorption Performance

The energy absorption parameters of the tested specimens, including EA , SEA , MCF and CFE , are presented in Table 3.2, and the energy absorption parameters of the two identical specimens are found to be close, which confirms the repeatability of the experimental data. The comparison of specimens with and without aluminum foam filler reveals that the aluminum foam filler can significantly improve the energy absorption performance in terms of the increase in EA , SEA , MCF and CFE . Further, EA , SEA and MCF generally exhibit increase as the volume of aluminum foam increases. The aluminum foam-filled specimens TTT, CCC, CTC and FFF exhibit 54.4%, 66.0%, 42.5% and 141.0% increase in EA (or MCF) as compared to the specimen without aluminum foam (NNN). The corresponding increase percentages of SEA are 42.7%, 45.5%, 27.2% and 97.2%, and the improvement in SEA by filling aluminum foam is due to higher SEA of aluminum foam as compared to nested tubes (as presented in Fig. 3.11). In addition, CFE of the energy absorber is also improved with the presence of aluminum foam filler, i.e., the specimens TTT, CCC, CTC and FFF exhibits 21.6, 45.3, 44.4 and 40.7% increase in CFE as compared to the specimen NNN. This indicates that the aluminum foam filler can effectively smooth the force–displacement curve and improve the energy absorption efficiency of the energy absorber.

Figure 3.11 presents the FE-predicted SEA values of nested tubes and aluminum foams of the specimens corresponding to crushing displacement of 63 mm. The SEA of nested tubes of the specimen FFF with fully-filled aluminum foam is found to be improved by 23.3% as compared to the specimen NNN. In addition, filling aluminum foam in triangular tubes (specimen TTT) also results in 5.9% increase of

Fig. 3.11 SEAs of nested tubes (SEAT) and aluminum foam (SEAF) from FE analyses, reprinted from Wang et al. (2021), copyright 2022, with permission from Elsevier

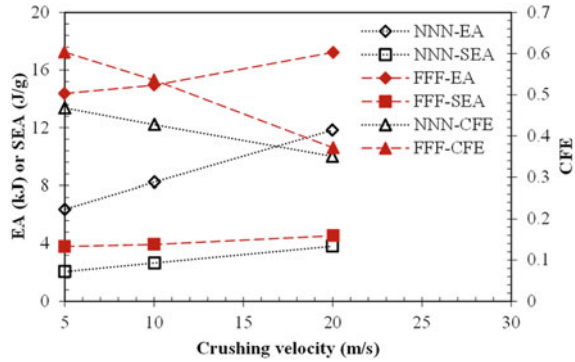


SEA of nested tubes. This indicates that the interaction effect between nested tubes and aluminum foam can enhance energy absorption performance of nested tubes for specimens FFF and TTT. Further, the specimen FFF with fully-filled aluminum foam exhibits highest *SEA* of nested tubes, indicating its more significant interaction effect between nested tubes and aluminum foam as compared to the other energy absorbers. With regard to *SEA* of aluminum foam, the highest value is observed for the specimen FFF (7.01 J/g), followed by specimens TTT and CCC (4.80 and 4.56 J/g, respectively). The specimen CTC exhibits lowest *SEA* of aluminum foam (3.32 J/g). Hence, it can be concluded that the AFCTNT energy absorber with fully-filled aluminum foam is superior to the other energy absorbers with partially-filled aluminum foam or without aluminum foam in terms of higher *SEA* of nested tubes and aluminum foam. This can be attributed to its more significant interaction effect between nested tubes and aluminum foam.

3.3.6 Further FE Analysis

During the drop-weight impact tests, different drop heights (or initial impact velocities) were chosen for different specimens in order to assure all the specimens reaching densification and the maximum impact force being smaller than 2000 kN. Herein, the FE simulations on the specimens FFF and NNN under the same crushing velocity are conducted in order to more fairly compare the performances of energy absorbers with and without aluminum foam filler. Moreover, three different crushing velocities are also adopted for the specimens FFF and NNN, including 5, 10 and 20 m/s, and the effect of crushing velocity on the energy absorption performance can be revealed. Figure 3.12 presents a comparison of energy absorption parameters of FFF and NNN under variant crushing velocity. Increasing crushing velocity is found to result in the evident increase in *EA* and *SEA*, but decrease in *CFE*. In addition, an almost linear variation of these energy absorption parameters to crushing velocity can be observed. The *EA* (or *SEA*) of FFF and NNN are increased by 19.8% and 85.7%, respectively, on increasing crushing velocity from 5 m/s to 20 m/s. This can

Fig. 3.12 Effect of crushing velocity on energy absorption performance, reprinted from Wang et al. (2021), copyright 2022, with permission from Elsevier



be attributed to the significant strain rate sensitivity of mild steel. It is also noted that the increase percentage of FFF with fully-filled aluminum foam is smaller than that of NNN without aluminum foam filler. This is because the aluminum foam generally exhibits strain rate insensitivity. Moreover, the inertial effect may also result in the increase in EA (or SEA) of FFF and NNN via changing deformation mode. Figure 3.12 also shows that the CFE of FFF and NNN is decreased by 38.5% and 17.2%, respectively, on increasing crushing velocity from 5 m/s to 15 m/s, which can be attributed to the increased peak buckling forces of the two energy absorbers. The comparison of energy absorption parameters of FFF and NNN indicates that the aluminum foam filled energy absorber (FFF) outperforms the one without aluminum foam (NNN) in terms of higher EA, SEA and CFE, which is mainly owing to the high SEA and smooth stress–strain relationship of aluminum foam.

To further confirm the superior performance of the AFCTNT energy absorber with aluminum foam filler, the FE simulations are conducted on two additional CTNT energy absorbers which have identical weight to the AFCTNT energy absorber via increasing the thickness of circular tube (NNN-C) and triangular tube (NNN-T), respectively. Figure 3.13 presents a comparison of energy absorption parameters of the three specimens with identical weight (i.e., FFF, NNN-C and NNN-T) under crushing velocity of 10 m/s. The specimen FFF is found to outperform the other two specimens without aluminum foam filler (NNN-C and NNN-T). With regard to EA (or SEA) of the three specimens, the highest value is observed for FFF, followed by NNN-T and NNN-C, owing to higher SEA of aluminum foam as compared to triangular and circular tubes. The laterally loaded triangular tube generally exhibits higher EA and SEA as compared to circular tube (Wang et al. 2020a), which results in higher EA and SEA of NNN-T with increased thickness of triangular tube as compared to NNN-C with increased thickness of circular tube. However, the crushing force–displacement curve of laterally loaded triangular tube is less smooth than that of circular tube, which generally yields a smaller CFE. Hence, the specimen NNN-T exhibits lowest CFE among the three specimens. It is known that increasing the thickness of laterally loaded tube can generally increase its SEA as the increase in EA of the tube is more significant as compared to the increase in weight via increasing

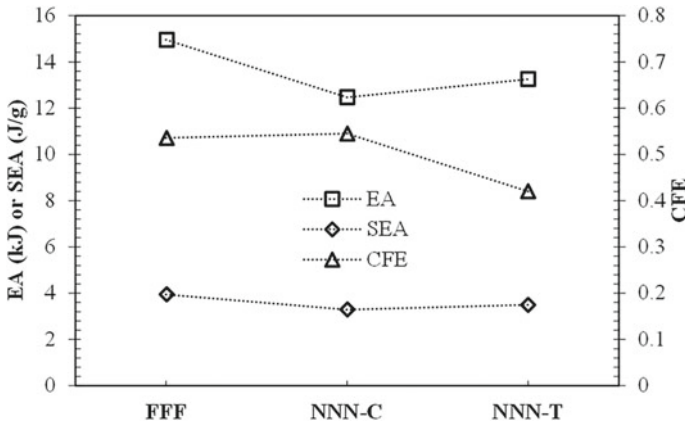


Fig. 3.13 Energy absorption parameters of FFF, NNN-C and NNN-T, reprinted from Wang et al. (2021), copyright 2022, with permission from Elsevier

thickness of the tube (Wang et al. 2020b). However, thicker tube may be more prone to fracture failure under severe crushing. With regard to aluminum foam, it exhibits both high *SEA* and smooth stress–strain relationship, which can be employed for improving the performance of “tube-type” energy absorbers.

3.4 Summary

In this chapter, a new AFCTNT energy absorber was proposed, and its energy absorption performance under impact loading was experimentally and numerically studied. The energy absorption parameters, deformation modes, and force–displacement responses of the AFCTNT energy absorbers were obtained by employing an instrumented drop-weight impact test system. In addition, numerical studies on the AFCTNT energy absorbers under impact loading were also performed to further reveal their impact responses and energy absorption performances. The main findings from the experimental and numerical studies were summarized as follows:

1. The variation in aluminum foam volume exhibited evident influence on the deformation modes and impact energy dissipation manners of AFCTNT energy absorbers. The aluminum foam filled in the gaps between circular and triangular tubes exhibited earlier impact energy dissipation as compared to that filled in triangular tubes.
2. Experimental results showed that the variation in aluminum foam volume also affected the force–displacement responses of the AFCTNT energy absorbers. The aluminum foam filled in the gaps between circular and triangular tubes was found to smooth the force–displacement curve of the energy absorber, thus resulting in higher energy absorption efficiency.

3. The energy absorption parameters of AFCTNT energy absorbers (*EA*, *SEA*, *MCF* and *CFE*) were found to be significantly improved by filling aluminum foam, and the AFCTNT energy absorbers filled with larger volume of aluminum foam generally exhibited higher energy absorption capacity.
4. The AFCTNT energy absorber with fully-filled aluminum foam was found to outperform the other AFCTNT energy absorbers with partially-filled aluminum foam or without aluminum foam in terms of higher *EA* and *SEA*, which could be attributed to more significant interaction effect between nested tubes and aluminum foam.
5. Numerical results showed that increasing crushing velocity could result in evident increase in *EA* and *SEA*, but decrease in *CFE*. In addition, the aluminum foam could be a desirable energy absorbing material to be filled in the CTNT energy absorber for enhancing its energy absorption performance.

References

- Ahmad Z, Thambiratnam DP (2009) Dynamic computer simulation and energy absorption of foam-filled conical tubes under axial impact loading. *Comput Struct* 87:186–197
- Baroutaji A, Arjunan A, Stanford M et al (2021) Deformation and energy absorption of additively manufactured functionally graded thickness thin-walled circular tubes under lateral crushing. *Eng Struct* 226:111324
- Baroutaji A, Gilchrist MD, Olabi AG (2016) Quasi-static, impact and energy absorption of internally nested tubes subjected to lateral loading. *Thin-Walled Struct* 98:337–350
- Baroutaji A, Gilchrist MD, Smyth D et al (2015) Analysis and optimization of sandwich tubes energy absorbers under lateral loading. *Int J Impact Eng* 82:74–88
- Baroutaji A, Sajjia M, Olabi AG (2017) On the crashworthiness performance of thin-walled energy absorbers: Recent advances and future developments. *Thin-Walled Struct* 118:137–163
- Duarte I, Vesenjok M, Krstulović-Opara L et al (2015) Static and dynamic axial crush performance of in-situ foam-filled tubes. *Compos Struct* 124:128–139
- Fan H, Hong W, Sun F et al (2015) Lateral compression behaviors of thin-walled equilateral triangular tubes. *International Journal of Steel Structures Int J Steel Struct* 15(4):85–795
- Fan Z, Shen J, Lu G et al (2013) Dynamic lateral crushing of empty and sandwich tubes, *Int J Impact Eng* 53:3–16
- Fang J, Gao Y, An X et al (2016) Design of transversely-graded foam and wall thickness structures for crashworthiness criteria. *Compos Part B: Eng* 92:338–349
- Gupta NK, Sekhon GS, Gupta PK (2001) A study of lateral collapse of square and rectangular metallic tubes, *Thin-Walled Struct* 39(9):745–772
- Gupta NK, Sekhon GS, Gupta PK (2005) Study of lateral compression of round metallic tubes. *Thin-Walled Struct* 43:895–992
- Hallquist JO (2006) LS-DYNA theory manual. Livermore Software Technology Corporation (LSTC). Livermore, California
- Hanssen AG, Hopperstad OS, Langseth M et al (2002) Validation of constitutive models applicable to aluminium foams, *Int J Mech Sci* 44:359–406
- Jones N (1988) *Structural Impact*. Cambridge University Press, Cambridge/New York
- Kilicaslan C (2015) Numerical crushing analysis of aluminum foam-filled corrugated single- and double-circular tubes subjected to axial impact loading. *Thin-Walled Struct* 96:82–94

- McDevitt TJ, Simmonds JG (2003) Crushing of an elastic-plastic ring between rigid plates with and without unloading. *J Appl Mech* 70:799–808
- Nikkhah H, Baroutaji A, Kazancı Z et al (2020) Evaluation of crushing and energy absorption characteristics of bio-inspired nested structures. *Thin-Walled Struct* 148:106615
- Morris E, Olabi AG, Hashmi MSJ (2006) Analysis of nested tube type energy absorbers with different indenters and exterior constraints. *Thin-Walled Struct* 44:872–885
- Olabi AG, Morris E, Hashmi MSJ et al (2008) Optimised design of nested oblong tube energy absorbers under lateral impact loading. *Int J Impact Eng* 35(1):10–26
- Qi C, Sun Y, Yang S (2018) A comparative study on empty and foam-filled hybrid material double-hat beams under lateral impact. *Thin-Walled Struct* 129:327–341
- Qi C, Yang S (2014) Crashworthiness and lightweight optimisation of thin-walled conical tubes subjected to an oblique impact. *Int J Crashworthiness* 19(4):334–351
- Santosa SP, Wierzbicki T, Hanssen AG et al (2000) Experimental and numerical studies of foam-filled sections. *Int J Impact Eng* 24:509–534
- Reddy TY, Reid SR (1979) Lateral compression of tubes and tube-systems with side constraints. *Int J Mech Sci* 21 (3):187–199
- Reid SR, Drew SLK, Carney JF (1983) Energy absorbing capacities of braced metal tubes, *Int J Mech Sci* 25(9–10):649–667
- Reyes A, Hopperstad OS, Langseth M (2004) Aluminum foam-filled extrusions subjected to oblique loading: experimental and numerical study. *Int J Solids Struct* 41:1645–1675
- Shahbeyk S, Petrinic N, Vafai A (2007) Numerical modelling of dynamically loaded metal foam-filled square columns. *Int J Impact Eng* 34:573–586
- Shen J, Lu G, Ruan D, Seah CC (2015) Lateral plastic collapse of sandwich tubes with metal foam core. *Int J Mech Sci* 91:99–109
- Song HW, Fang ZJ, Yu G et al (2005) Partition energy absorption of axially crushed aluminium foam-filled hat sections. *Int J Solids Struct* 42(9):2575–2600
- Su XY, Yu TX, Reid SR (1995a) Inertia-sensitive impact energy-absorbing structures part I: effects of inertia and elasticity. *Int J Impact Eng* 16(4):651–672
- Su XY, Yu TX, Reid SR (1995b) Inertia-sensitive impact energy-absorbing structures part II: effects of strain rate. *Int J Impact Eng* 16(4):673–689
- Tran T (2017) Crushing analysis of multi-cell thin-walled rectangular and square tubes under lateral loading. *Compos Struct* 160:734–747
- Tran T, Ton TNT (2016) Lateral crushing behaviour and theoretical prediction of thin-walled rectangular and square tubes, *Compos Struct* 154:374–384
- Tran TN, Baroutaji A, Estrada Q et al (2021) Crashworthiness analysis and optimization of standard and windowed multi-cell hexagonal tubes. *Struct Multidisc Optim* 63:2191–2209
- Wang CY (1987) Crushing of an elastic-perfectly plastic ring or tube between two planes. *J Appl Mech* 54:159–164
- Wang P, Zheng Q, Fan H et al (2015) Quasi-static crushing behaviors and plastic analysis of thin-walled triangular tubes. *J Constr Steel Res* 106:35–43
- Wang Y, Lu J, Zhai X et al (2019) Response of energy absorbing connector with polyurethane foam and multiple pleated plates under impact loading. *Int J Impact Eng* 133:103356
- Wang Y, Zhai X, Liu S et al (2020a) Energy absorption performance of a new circular-triangular nested tube and its application as sacrificial cladding. *Thin-Walled Struct* 106992
- Wang Y, Zhang B, Lu J et al (2020b) Quasi-static crushing behaviour of the energy absorbing connector with polyurethane foam and multiple pleated plates. *Eng Struct* 211:110404
- Wang Y, Zhang R, Liu S et al (2021) Energy absorption behaviour of an aluminium foam-filled circular-triangular nested tube energy absorber under impact loading. *Structures* 34:95–104
- Wu L, Carney JF (1997) Initial collapse of braced elliptical tubes under lateral compression. *Int J Mech Sci* 39(9):1023–1036
- Yang S, Qi C (2013) Multiobjective optimization for empty and foam-filled square columns under oblique impact loading. *Int J Impact Eng* 54:177–191